Diffusion quantum Monte Carlo approach to the polaritonic ground state

Braden M. Weight [1,2,*] Sergei Tretiak,[2] and Yu Zhang [2,†]

[1]*Department of Physics and Astronomy, University of Rochester, Rochester, New York 14627, USA*
[2]*Theoretical Division, Los Alamos National Laboratory, Los Alamos, New Mexico 87545, USA*

Making and using polaritonic states (i.e., hybrid electron-photon states) for chemical applications has recently become one of the most prominent and active fields that connects the communities of chemistry and quantum optics. Modeling of such polaritonic phenomena using *ab initio* approaches calls for new methodologies, leading to the reinvention of many commonly used electronic structure methods, such as Hartree-Fock, density functional, and coupled cluster theories. In this work, we explore the formally exact diffusion quantum Monte Carlo approach to obtain numerical solutions to the polaritonic ground state during the dissociation of the H_2 molecular system. We examine various electron-nuclear-photon properties throughout the dissociation, such as changes to the minimum of the cavity Born-Oppenheimer surface, the localization of the electronic wave function, and the average mode occupation. Finally, we directly compare our results to that obtained with state-of-the-art, yet approximate, polaritonic coupled cluster approaches.

I. INTRODUCTION

Recent experimental studies of highly entangled light-matter states, known as polaritons, have demonstrated their ability to modify chemical reactions [1–12] and physical properties [13–19] of both low- and high-dimensional material systems [20–27]. This has garnered a substantial interest in the theoretical community [28–32]. Specifically, computational chemists have devoted the past few years to the "regeneration" of various many-body methods—ubiquitously applied to pristine many-electron systems—for use in the case of strongly correlated electron-photon systems [28,30,33]. All these approaches attempt to solve a nonrelativistic quantum electrodynamic (QED) Hamiltonian for the coupled electron-nuclear-photon system for its eigenstates, usually within the cavity Born-Oppenheimer approximation [34–36], being the case for most conventional electronic structure methods. These modified self-consistent (sc) approaches include the scQED Hartree-Fock (scQED-HF) [35,37,38], density functional theory (scQED-DFT) [39–43], coupled cluster theory (scQED-CC) techniques [37,44–46], and Møller-Plesset perturbation theory (scQED-MP2) [47], to name a few. Moreover, the analogous methods for excited-state simulations have also been recently developed, such as time-dependent scQED-DFT (scQED-TDDFT) [48–53], equation of motion scQED-CC (scQED-EOMCCSD) [46,51,54], and complete active space configuration interaction (scQED-CASCI) [55].

In many of these cases, the drawbacks of the original method are exacerbated in its scQED analog. For example, to describe the electron-photon correlations in the DFT approach, new exchange-correlation functionals needs to be constructed to explicitly account for such effects [39,40,43,56–58]. The early attempts at developing such functionals resulted in a dramatic reduction in the quality of treatment of bare electron-electron correlations [36,44,45,52,53]. While efforts toward constructing improved functionals for the scQED-DFT approach are ongoing with marked success [57,58], the "exact" effects of the cavity presence on the electronic subsystem are only trustworthy up to the choice of electron-photon and electron-electron exchange-correlation functionals.

One promising approach is the scQED-CC method, which adds correlation on top of the scQED-HF approach. Here the electron-electron correlations are treated by including single and double excitations, which is known to provide accurate results, even for highly correlated many-electron systems. In fact, the CCSD approach is exact for two-electron systems in the absence of the cavity since the single and double excitations comprise the full configuration interaction limit (up to the choice of basis set). This is no longer valid when the cavity is present, since the cavity photons can be excited to an arbitrary level due to their bosonic nature [54]. Due to the large computational expense, the scQED-CC method has only been used for small molecular systems coupled to the cavity with typically one or two photonic excitations included. This approach is expected to provide reliable results, even for large light-matter coupling strengths [37,45]. However, such truncation of the photonic excitations has been shown to contradict the full configuration interaction limit in the strong-coupling regimes for simple Hubbard model systems, even when using up to 10 photonic excitations [54]. Notably, this high-level photonic treatment is usually numerically intractable for models describing realistic molecular systems.

State-of-the-art experimental designs using plasmonic nanocavities have already shown strong coupling at moderate conditions [59,60]. These recent advancements in cavity

---

*bweight@ur.rochester.edu
†zhy@lanl.gov

design lead the way for novel chemistry of cavity-modified chemistry. In response to these experimental strides, much recent theoretical progress has been made focusing on the strong coupling of plasmonic cavities to the ground-state potential energy surface of various molecular systems (at high cavity frequencies on the order of electronic transitions ∼1– 20 eV), showcasing changes in the ground-state electronic density [37,46], modifications to nonbonded interaction potentials [44], electron affinities of diatomic molecules [46], as well as a more complicated exploration of the cavity-induced modifications to reaction barriers in proton-transfer reactions [21,36,45,47].

To our knowledge, the experimental realization of cavity-induced changes to the polaritonic ground state through coupling to high-frequency electronic transitions has yet to be achieved. However, we hypothesize that such experiments are expected within the next few years. Some examples of experiments that may provide insight are linear and nonlinear spectroscopies (e.g., infrared, Raman, pump-probe, etc.) of the polaritonic ground state with cavity-coupled molecules, which have already been done for low-frequency cavity designs aimed at the exploration of vibropolaritons [11,28]. We hypothesize that these experiments will provide direct insight into the modifications of the ground-state potential energy surfaces and the resulting changes to the vibrational/nuclear system. Such changes to the excited-state potential energy surfaces have already been widely observed in experiment [61–65].

In this work, we explore the polaritonic ground state of the H_2 molecular system coupled to a single quantized cavity mode. These interactions between light and matter are often called QED vacuum fluctuations and become important in the presence of a matter which causes a polarization of the cavity mode [66–68]. We solve the Pauli-Fierz QED Hamiltonian in the long-wavelength approximation using the diffusion quantum Monte Carlo (DQMC) approach. This methodology converges to the exact solution for the two-electron H_2 molecular system, even when many quantized photonic modes are considered. We then directly compare with state-of-the-art polaritonic coupled cluster methods to highlight the inherent approximations in such schemes. Various properties are examined, such as the localization of the electronic wave function and changes to the polaritonic potential energy surface. We also explore a decomposition of the photonic wave functions into the number (or Fock) basis. This analysis highlights the discrepancy between the scQED-CCSD and DQMC results due to the inclusion of high-level photonic excitations present even in the ground state. Finally, we examine the average photon number as a function of the nuclear separation length. Our results suggest the DQMC scheme as another chemically relevant approach toward modeling molecular and material systems inside the cavity.

II. METHODOLOGY

A. Electronic Hamiltonian

The molecular Hamiltonian,

$$\hat{H}_M = \hat{T}_N + \hat{T}_{el} + \hat{V} = \hat{T}_N + \hat{H}_{el}, \tag{1}$$

consists of the nuclear kinetic energy, $\hat{T}_N$, the electronic kinetic energy, $\hat{T}_{el}$, and all pairwise Coulomb interactions, $\hat{V} = \hat{V}_{ee} + \hat{V}_{eN} + \hat{V}_{NN}$, between electrons e and nuclei N. The electronic Hamiltonian, $\hat{H}_{el} = \hat{H}_M - \hat{T}_N$, which is approximately solved by a number of electronic structure software, can be written as an eigenvalue problem and yields the Born-Oppenheimer approximation for the electronic states parametrized by the nuclear positions,

$$\hat{H}_{el}|\psi_j(\mathbf{R})\rangle = E_j|\psi_j(\mathbf{R})\rangle. \tag{2}$$

In this work, we consider a "simple" two-electron H_2 molecular system and its interatomic dissociation inside and outside a photonic cavity. In this case, the electronic Hamiltonian takes the form

$$\hat{H}_{el} = \frac{\hat{\mathbf{p}}_1^2}{2} + \frac{\hat{\mathbf{p}}_2^2}{2} + \frac{1}{|\hat{\mathbf{r}}_1 - \hat{\mathbf{r}}_2|} - \frac{1}{|\hat{\mathbf{r}}_1 - \mathbf{R}_1|} - \frac{1}{|\hat{\mathbf{r}}_1 - \mathbf{R}_2|}$$
$$- \frac{1}{|\hat{\mathbf{r}}_2 - \mathbf{R}_1|} - \frac{1}{|\hat{\mathbf{r}}_2 - \mathbf{R}_2|} + \frac{1}{|\mathbf{R}_1 - \mathbf{R}_2|}, \tag{3}$$

where $\{\mathbf{R}_1, \mathbf{R}_2\} = \mathbf{R}$ denote the nuclear coordinates, and $\{\hat{\mathbf{r}}_1, \hat{\mathbf{r}}_2\}$ and $\{\hat{\mathbf{p}}_1, \hat{\mathbf{p}}_2\}$ are the position and momenta operators of the electrons, respectively. Solving Eq. (2) yields the electronic adiabatic states $|\psi_j(\mathbf{R})\rangle$, their respective eigenenergies $E_j(\mathbf{R})$, and all subsequent properties. As a matter of notation, we will drop the dependence on $\mathbf{R}$ from the adiabatic wave functions $|\psi_j(\mathbf{R})\rangle \equiv |\psi_j\rangle$ and the adiabatic energies $E_j(\mathbf{R}) \equiv E_j$ for brevity. Achieving an exact solution has proven to be challenging, even for the state-of-the-art approximate many-body methods, such as density functional theory (DFT). Exact diagonalization of this Hamiltonian requires the solution of a six-dimensional Hilbert space, and it can be accomplished via coupled cluster singles and doubles (CCSD), which coincides with the full configuration interaction (FCI) limit for this two-electron system.

B. Diffusion Monte Carlo

In many cases, the approximate solution to a high-dimensional integral problem can be achieved using a Monte Carlo approach, which leverages the concept of random variables in high-dimensional space. Monte Carlo integration is ubiquitous in the community for both classical and quantum mechanical problems, when the number of degrees of freedom (DOFs) is large. One of the most common approaches is Markov-Chain Monte Carlo based on the Metropolis-Hastings algorithm [69], which is related to the variational quantum Monte Carlo (VQMC) [70], and it is used to solve for the equilibrium distribution of the many-particle system.

In this work, we focus on a particular quantum mechanical analog called diffusion quantum Monte Carlo (DQMC) [71–77]. In DQMC, the wave function is approximated by a basis of random walkers whose "motion" is defined by multiple applications of a short-time Green's function for the Schrödinger equation in imaginary time.

The imaginary time Schrödinger equation, in the six-dimensional real-space basis, can be written as

$$\frac{\partial}{\partial \tau}\psi(\mathbf{r}, \tau) = \left(\frac{1}{2}\nabla_{\mathbf{r}}^2 + V(\mathbf{r})\right)\psi(\mathbf{r}, \tau), \tag{4}$$

where $\tau = it$ and $\frac{1}{2}\nabla_{\mathbf{r}}^2 = \frac{1}{2}\nabla_{\mathbf{r}_1}^2 + \frac{1}{2}\nabla_{\mathbf{r}_2}^2$. Specifically, $\mathbf{r} = (\mathbf{r}_1, \mathbf{r}_2)$ is a single point in the six-dimensional configuration space of the two electrons in H_2. Note that the nuclear positions $\mathbf{R}$ [see Eq. (1)] are kept fixed and contribute to the total potential $V(\mathbf{r}; \mathbf{R})$ and the adiabatic wave functions $|\psi(\mathbf{r}, \mathbf{R})\rangle$ but are dropped from the notation for brevity. The formal solution of this equation can be written as a Green's function,

$$\psi(\mathbf{r}, \tau) = \int d\mathbf{r}' \, G(\mathbf{r}, \mathbf{r}', \tau)\psi(\mathbf{r}', 0). \tag{5}$$

This propagator $G(\mathbf{r}, \mathbf{r}', \tau)$ can be approximated by the Trotter-Suzuki splitting of the time-evolution operator as [78,79]

$$e^{[\frac{1}{2}\nabla_{\mathbf{r}}^2 + V(\mathbf{r})]d\tau} \approx e^{\frac{1}{2}\nabla_{\mathbf{r}}^2 d\tau} e^{V(\mathbf{r})d\tau} \tag{6}$$

during a short-time interval $d\tau = \frac{\tau}{N_{\text{steps}}}$ leading to the following Green's function approach:

$$G(\mathbf{r}, \mathbf{r}', \tau) = \lim_{d\tau \to 0}[G_{\text{diff}}(\mathbf{r}, \mathbf{r}', d\tau)$$
$$\times G_{\text{Birth/Death}}(\mathbf{r}, \mathbf{r}', d\tau)]^{N_{\text{steps}}}. \tag{7}$$

The formal solutions to these Green's functions are

$$G_{\text{diff}}(\mathbf{r}, \mathbf{r}', d\tau) = e^{-\frac{(\mathbf{r}-\mathbf{r}')^2}{2d\tau}} \tag{8}$$

$$G_{\text{Birth/Death}}(\mathbf{r}, \mathbf{r}', d\tau) = e^{-d\tau \frac{V(\mathbf{r})+V(\mathbf{r}')}{2}}. \tag{9}$$

Here, and in the equations above, $\mathbf{r}$ and $\mathbf{r}'$ are two system configurations of the $(3N_{\text{el}})$-dimensional space (the nuclear DOFs are fixed), where N_{el} is the number of electrons ($N_{\text{el}} = 2$ in this case). The first Green's function is the solution to the diffusion equation in free space (i.e., $\partial_\tau \psi = \frac{1}{2}\nabla^2\psi$), which leads to an unbiased Gaussian random walk with a standard deviation $\sqrt{\tau}$.

The second propagator gives rise to an exponential probability of the random walker itself, often called the Birth/Death algorithm. This propagator dictates the multiplication or destruction of a walker according to the probability distribution $\mathcal{P}_w \sim G_{\text{Birth/Death}}(\mathbf{r}', \mathbf{r}, \tau)$, given the current $V(\mathbf{r}')$ and previous $V(\mathbf{r})$ total potential energies (for a single configuration of particles) of the system with configurations $\mathbf{r}'$ and $\mathbf{r}$, respectively. This term gives rise to a variable number of Gaussian random walkers, which can lead to an exponential increase (or decrease) of the number of walkers.

For practical reasons, one introduces an energy shift, E_T in Eq. (2), by replacing the energy eigenvalue E_j with $E_j - E_T$, where E_T is called the trial energy. The trial energy becomes an estimate of the exact ground-state energy after sufficient simulation time, $\lim_{\tau \to \infty} E_T(\tau) \approx E_0$. As such, this parameter is dynamic and can be understood as a solution to a first-order rate equation for the number of Gaussian random walkers N_w,

$$N_w(\tau + d\tau) = N_w(\tau)e^{-[E_T(\tau) - E_T(\tau + d\tau)]d\tau} = \bar{N}_w$$

$$\Rightarrow E_T(\tau + d\tau) = E_T(\tau) + \alpha \ln\left(\frac{\bar{N}_w}{N_w(\tau)}\right), \tag{10}$$

where α and $\bar{N}_w$ are parameters. $\bar{N}_w$ is the target number of random walkers (taken to be 10^6 in this work). $N_w(\tau = 0) = \bar{N}_w$ to initiate the simulation. α is a parameter that controls the stiffness of the variation in the number of random walkers. In
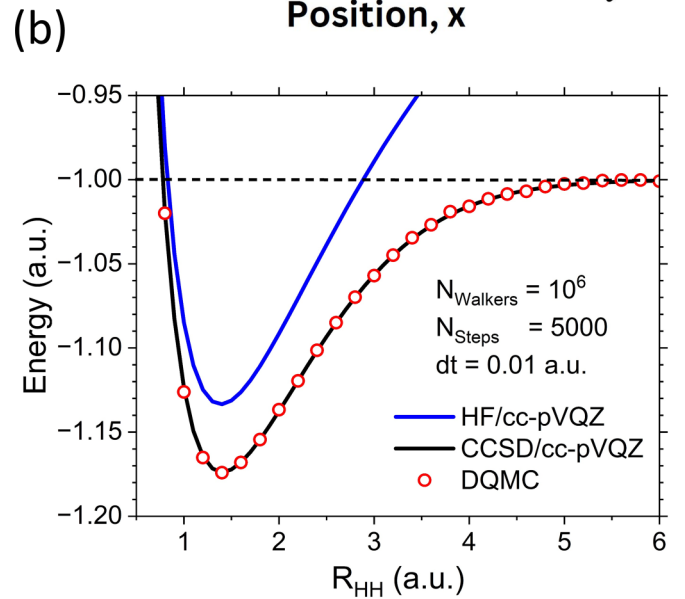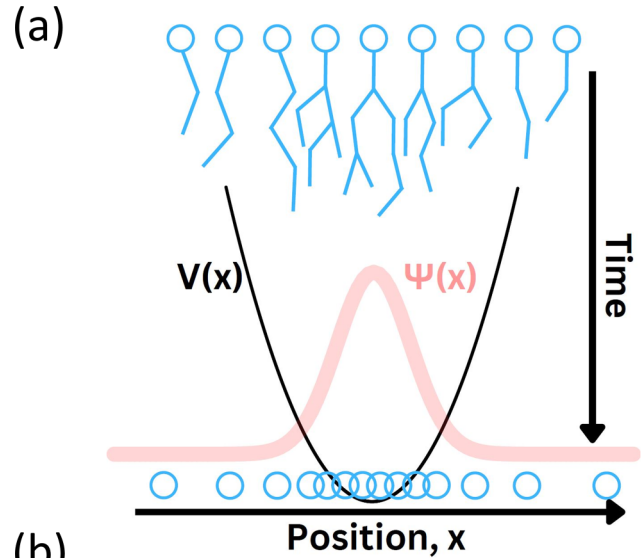

FIG. 1. (a) A schematic of the diffusion Monte Carlo process. Random walkers are initially sampled from a uniform distribution (top blue circles) and move in time (top-to-bottom) by a Gaussian random walk. At each step, the random walker may be removed or duplicated according to the potential energy landscape. (b) The ground-state potential energy surface of the H_2 dissociation outside the cavity at various computational levels: Hartree-Fock (HF, blue curve), coupled cluster singles doubles (CCSD, black curve), and diffusion quantum Monte Carlo (DQMC, red circles). The horizontal dashed black line indicates the exact dissociation energy of $E_{\text{diss}} = -1.0$ a.u.

this work, we choose $\alpha = 0.01$ a.u., which damps the oscillations in the number of walkers while still allowing them to fluctuate according to the birth/death Green's function without encountering numerical issues such as zero or infinite walkers. A schematic representation of the DQMC method is provided in Fig. 1(a).

The DQMC scheme converges to the exact solution for all nodeless ground states, which encompasses up to two fermions (e.g., electrons) and, in principle, an infinite number of bosons (e.g., photon modes). It is crucial to emphasize

that all results presented in this work converge to the exact answer since we restrict our study to no more than two electrons. This convergence is ensured when a sufficiently small propagation time step $d\tau$ is chosen and an adequate number of Gaussian random walkers N_w is used. Extensions of this scheme to ground states that have nodes (or phase changes) and to excited states have been well-studied for electronic systems. This augmentation often involves the fixed-node approximation, which necessitates *a priori* knowledge of the wave function's nodal structure. This structure is typically derived from a Hartree-Fock Slater determinant or its post-Hartree-Fock counterparts.

C. Pauli-Fierz Hamiltonian

The coupling between light and molecular DOFs can take many forms. In this work, we examine the interaction between the H_2 molecular system with a single quantized radiation mode (although there is no limit to the number of modes) using the Pauli-Fierz QED Hamiltonian [28,30] within the Born-Oppenheimer approximation (i.e., neglecting the nuclear kinetic energy $\hat{T}_R$). Mathematically, this Pauli-Fierz Hamiltonian can be written as

$$\hat{H}_{PF} = \hat{H}_{el} + \omega_c\left(\hat{a}^\dagger \hat{a} + \tfrac{1}{2}\right) + \omega_c A_0(\hat{\boldsymbol{\mu}} \cdot \hat{e})(\hat{a}^\dagger + \hat{a}) + \omega_c A_0^2(\hat{\boldsymbol{\mu}} \cdot \hat{e})^2, \tag{11}$$

where the second term represents the bilinear light-matter coupling term ($\hat{H}_{el\text{-}ph}$), and the third term denotes the dipole self-energy (DSE) ($\hat{H}_{DSE}$). The interactions between light and matter DOFs are controlled by the molecular dipole operator,

$$\hat{\boldsymbol{\mu}}(\hat{\mathbf{r}}) = -\sum_p^{N_{el}} \hat{\mathbf{r}}_p + \sum_I^{N_{IONS}} Z_I \mathbf{R}_I, \tag{12}$$

and its square,

$$\hat{\boldsymbol{\mu}}^2(\hat{\mathbf{r}}) = \sum_{p,p'}^{N_{el}} \hat{\mathbf{r}}_p \hat{\mathbf{r}}_{p'} - 2\sum_p^{N_{el}} \sum_I^{N_{IONS}} Z_I \hat{\mathbf{r}}_p \mathbf{R}_I + \sum_{I,I'}^{N_{IONS}} Z_I Z_{I'} \mathbf{R}_I \mathbf{R}_{I'}, \tag{13}$$

which encapsulates both one- and two-electron quadrupole-like terms. As will become clear in the next section, we require the light-matter Hamiltonian in the position representation for the cavity photon mode. Consequently, the Pauli-Fierz Hamiltonian can be rewritten as

$$\hat{H}_{PF} = \hat{H}_{el} + \tfrac{1}{2}\hat{p}_c^2 + \tfrac{1}{2}\omega_c^2 \hat{q}_c^2 + \sqrt{2\omega_c^3} A_0 \hat{\mu} \hat{q}_c + \omega_c A_0^2 \hat{\mu}^2, \tag{14}$$

where $\hat{q}_c = \sqrt{\frac{1}{2\omega_c}}(\hat{a}^\dagger + \hat{a})$ and $\hat{p}_c = \sqrt{\frac{\omega_c}{2}}(\hat{a}^\dagger - \hat{a})$ represent the position and momentum operators for the cavity photon.

D. Polaritonic diffusion Monte Carlo

While DQMC has been proven to exactly solve the ground state of bosonic systems, its extension toward entangled boson-fermion systems, particularly those arising from the strong coupling of molecular systems to light in optical or plasmonic cavities, remains underexplored. Nevertheless, extending this method to account for one or several quantized cavity or plasmonic modes is relatively straightforward using a similar approach by decomposing the exact Green's function into multiple short-time propagators for both the electronic and photonic DOFs.

Namely, we start from the imaginary-time Schrödinger equation for the Pauli-Fierz Hamiltonian in the position representation for both the electrons $\mathbf{r}$ and cavity mode q_c,

$$\frac{\partial}{\partial\tau}\psi(\mathbf{r}, q_c, \tau)$$

$$= \left(\frac{\nabla_\mathbf{r}^2}{2} + V(\mathbf{r}) + \frac{\nabla_{q_c}^2}{2} + V_{el-ph}(\mathbf{r}, q_c) + V_{DSE}(\mathbf{r})\right)$$

$$\times \psi(\mathbf{r}, q_c, \tau), \tag{15}$$

where $\mathbf{r}$ again signifies all six real-space coordinates of two electrons. The many-body "local" dipole for a specific configuration, $\mathbf{r}$, can be written as

$$\boldsymbol{\mu}(\mathbf{r}) = -\sum_p^{N_{el}} \mathbf{r}_p + \sum_I^{N_{IONS}} \mathbf{R}_I, \tag{16}$$

and the subsequent one- and two-electron quadrupole is

$$\boldsymbol{\mu}^2(\mathbf{r}) = \sum_{p,p'}^{N_{el}} \mathbf{r}_p \mathbf{r}_{p'} - 2\sum_p^{N_{el}} \sum_I^{N_{IONS}} Z_I \mathbf{r}_p \mathbf{R}_I + \sum_{I,I'}^{N_{IONS}} Z_I Z_{I'} \mathbf{R}_I \mathbf{R}_{I'}, \tag{17}$$

where p and p' label electrons, and I and I' denote nuclei. It is worth noting that the nuclear charge Z_I is 1, $N_{IONS} = 2$, and $N_{el} = 2$ for the H_2 cavity system.

Utilizing the Trotter expansion, the kinetic energy of the electrons and photon can be split into one short-time Green's function propagator, while the potential terms can be split into another set as

$$e^{\left[\frac{\nabla_\mathbf{r}^2}{2} + V(\mathbf{r}) + \frac{\nabla_{q_c}^2}{2} + V_{el-ph}(\mathbf{r},q_c) + V_{DSE}(\mathbf{r})\right]d\tau} \tag{18}$$

$$\approx e^{\left(\frac{\nabla_\mathbf{r}^2}{2} + \frac{\nabla_{q_c}^2}{2}\right)d\tau} e^{[V(\mathbf{r}) + V_{el-ph}(\mathbf{r},q_c) + V_{DSE}(\mathbf{r}) - E_T]d\tau}$$

$$\approx e^{\left(\frac{\nabla_\mathbf{r}^2}{2} + \frac{\nabla_{q_c}^2}{2}\right)d\tau} e^{[V_{Total}(\mathbf{r},q_c) - E_T]} \tag{19}$$

over a short-time interval $d\tau$. Here, $V_{Total}(\mathbf{r}, q_c) = V(\mathbf{r}) + V_{el-ph}(\mathbf{r}, q_c) + V_{DSE}(\mathbf{r})$ encompasses all the potential terms. We have also integrated the trial energy E_T directly into the above expression. This leads to the following Green's function approach for the coupled electron-photon system:

$$G(\mathbf{r}, q_c, \mathbf{r}', q_c', \tau) = \lim_{d\tau \to 0}[G_{diff}(\mathbf{r}, q_c, \mathbf{r}', q_c', d\tau)$$

$$\times G_{Birth/Death}(\mathbf{r}, q_c, \mathbf{r}', q_c', d\tau)]^{N_{steps}}. \tag{20}$$

In this case, the inclusion of the photonic DOF is formally analogous to an additional effective electronic one with a modified configurational potential energy $V(\mathbf{r}) \to V(\mathbf{r}) + V_{el-ph}(\mathbf{r}, q_c) + V_{DSE}(\mathbf{r}) = V_{Total}(\mathbf{r}, q_c)$ dependent on its position q_c and the configurational electronic dipole $\mu(\mathbf{r})$ as well as its square $\mu^2(\mathbf{r})$.

The formal solutions to these Green's functions are

$$G_{\text{Diff.}}(\mathbf{r}, q_c, \mathbf{r}', q_c', d\tau) = e^{-\frac{|\mathbf{r}-\mathbf{r}'|^2}{2d\tau}} e^{-\frac{(q_c-q_c')^2}{2d\tau}} \qquad (21)$$

$$G_{\text{Birth/Death}}(\mathbf{r}, q_c, \mathbf{r}', q_c', d\tau) = e^{-d\tau\left(\frac{V_{\text{Total}}(\mathbf{r},q_c)-V_{\text{Total}}(\mathbf{r}',q_c')}{2}-E_T\right)}. \qquad (22)$$

Updating the trial energy E_T follows the same procedure as with photon-free propagation [Eq. (10)]. The coupled electron-photon wave function is constructed by binning Gaussian random walkers at each time step into a set of equally sized histograms (i.e., shared by all time steps) such that the creation or destruction of walkers does not affect the histogram binning. Normalization is enforced at the end of the simulation.

E. Computational details

For clarity, we present a step-by-step breakdown of the proposed algorithm:

(1) Generate initiate configurations by uniformly sampling all DOFs (electronic array size: N_w walkers $\times$ N_{el} electrons $\times$ 3 dimensions; photonic array size: N_w walkers $\times$ N_{modes}) over a wide enough range, taking special case to sample initial configurations well beyond the nuclear distribution.

(2) Evaluate the total potential energy of the system for each configuration $V_{\text{Total}}(\mathbf{r}, q_c)$.

(3) Displace all walkers by sampling a Gaussian distribution with a standard deviation of $\sqrt{d\tau}$.

(4) Evaluate the total potential energy $V_{\text{Total}}(\mathbf{r}, q_c)$ for the updated configurations.

(5) Update the trial energy E_T according to Eq. (10).

(6) Calculate walker probabilities as

$$\mathcal{P}_w = \exp\left[-d\tau\left(\frac{V_{\text{Total}}(\mathbf{r}, q_c) + V_{\text{Total}}(\mathbf{r}', q_{c'})}{2} - E_T\right)\right].$$

(7) For each walker, compare its probability $\mathcal{P}_w$ to a unique uniform random number ξ and perform one of the following actions:

    (a) Kill the walker if $\mathcal{P}_w < \xi$.

    (b) Retain the walker if $\xi < \mathcal{P}_w < 1$.

    (c) Clone the walker if $\mathcal{P}_w > 1$.

(8) Repeat steps 3–5 until the requested number of steps is completed.

(9) Repeat steps 2–6 using the final configurations as the initial configurations for the primary or "production" simulation. Save all average energies and accrue configurational histograms (i.e., the wave function) during the production simulation.

Unless otherwise noted, all data reported here use $N_w = 10^6$ walkers, $N_{\text{steps}} = 5000$ steps for the equilibration as well as for the production simulations, $N_{\text{el}} = 2$ electrons, and $N_{\text{modes}} = 1$ cavity mode. We adopt a numerical time step of $d\tau = 0.01$ a.u. and a population parameter of $\alpha = 0.01$ a.u. A statistical analysis was performed on the resulting dynamics to account for the serial correlation present in the random walkers [80–82]. We refer the interested reader to Figs. S1–S3 and their discussion in the supplemental material [83].

III. RESULTS AND DISCUSSION

A. Bare H$_2$ dissociation

The dissociation potential energy surface (PES) of bare H$_2$, defined as the ground-state energy $E(\mathbf{R})$ as a function of the H-H distance ($\mathbf{R}$), has been a common benchmark for new many-body methods as well as new density functionals for its simultaneous simplicity and complexity. The ground-state reaction can be thermally activated given sufficient kinetic energy at a finite temperature to overcome or tunnel through the reaction barrier. Given the two-electron constitution, the Born-Oppenheimer surface can be computed exactly using CCSD in the complete basis limit. In contrast, approximate methods, such as Hartree-Fock confined to the mean-field level of electron-electron correlation, perform very poorly for the H$_2$ dissociation. This can be improved using the broken-symmetry solution (i.e., performing an unrestricted self-consistent field Hartree-Fock analog). However, such a solution, while improving the energy landscape of the mean-field solution, fails to capture precise symmetries of the electron orbitals. Hence, the physical nature of the wave function still requires further corrections.

From this perspective, CCSD and HF results comprise the best and worst limits of *ab initio* approaches toward the H$_2$ dissociation, respectively, and will serve as a reference for the current diffusion quantum Monte Carlo (DQMC) study. Figure 1(b) presents the results of the HF, CCSD, and DQMC methods for the pristine (i.e., no cavity) H$_2$ dissociation. The HF and CCSD results are obtained using the PySCF [84,85] electronic structure package using the cc-pVQZ basis set. For the DQMC results, the standard deviations of the mean energy are shown as vertical error bars for each nuclear separation length.

In this case, we find that the DQMC approach agrees well with the reference CCSD results. In the case of two electrons, CCSD is expected to perform well, contingent solely on the choice of basis set. However, introduction of the cavity photon mode when incorporating polaritons leads to harsh approximations in the treatment of both bare photonic excitation and coupled excitations. These truncations in the polaritonic CCSD (or scQED-CCSD) have been comprehensively discussed in the existing literature [28,30,37,44–46,51,54].

B. Polaritonic dissociation curves

In the presence of the cavity, the ground-state PES, and consequently the reaction barrier, of a molecule can be altered due its coupling cavity [32,36,37,44,45,47,66]. In this work, we examine the effect of the cavity on the ground-state PES at different coupling strengths A_0 and photon frequencies ω_c. Figure 2 presents the primary results of this work: the polaritonic potential energy surfaces of the H$_2$ dissociation at varied light-matter coupling strengths A_0 (colors) and cavity frequencies ω_c. For each simulation (i.e., symbol), the standard deviation of the mean energy is shown by a vertical error bar. The horizontal dashed line indicates the expected dissociation energy at zero light-matter coupling, which is computed as the dissociation energy outside the cavity E_{diss} and the zero-point energy (ZPE) of the cavity mode $E_{\text{ZPE}} = \frac{1}{2}\omega_c$.
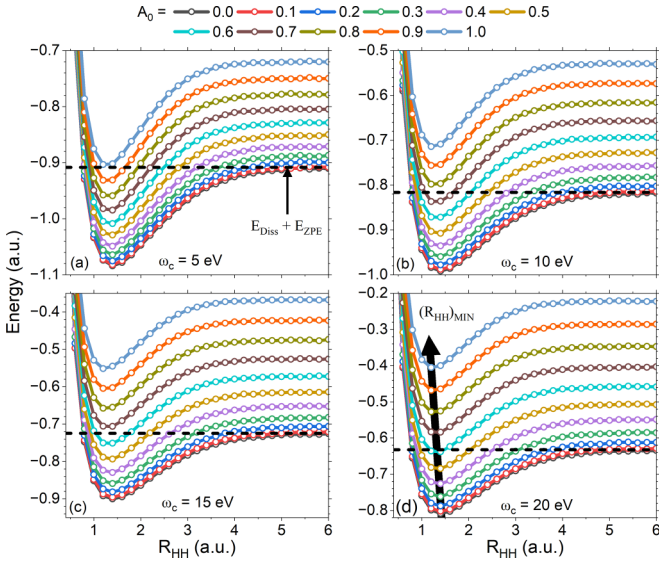
FIG. 2. Potential energy surfaces for the ground state H_2 dissociation at various coupling strengths A_0 from 0.0 to 1.0 a.u. in increments of 0.1 a.u. (from bottom to top) for four cavity frequencies $\omega_c = 5.0$ (a), 10.0 (b), 15.0 (c), and 20.0 (d) eV. The horizontal dashed line references the expected dissociation energy with vanishing light-matter coupling calculated as $E_{diss} + \frac{1}{2}\omega_c$. The cavity polarization is parallel to the bond axis. The black arrow in panel (d) highlights the shift of the minimum energy point $(R_{HH})_{MIN}$ in the potential energy surfaces to lower values with increasing light-matter coupling strength A_0.

Two prominent features can be observed immediately: (I) the vertical energy shift with increasing light-matter coupling strength A_0, and (II) the shift of the minima to lower values of R_{HH}. This first observation is expected, since the primary contribution to the ground-state energy is given by the DSE term, which only adds positive values to the total potential energy for each configuration. The second observation is, however, more interesting, since even small changes to such adiabatic surfaces may give rise to a wide range of modified chemistry, e.g., the bond stiffness during a chemical reaction, and the nonadiabatic couplings between electronic states in photoexcited processes. These phenomena can be monitored by specific spectroscopic signatures, either in the ground (e.g., infrared/Raman) or excited states (e.g., absorption/emission).

The shift of the minimum in the potential energy surface as a function of the light-matter coupling strength A_0 is presented in Fig. 3(a). The results are plotted as an average over all four cavity frequencies ($\omega_c = 5.0$, 10.0, 15.0, and 20.0 eV), given the minimal frequency dependency observed. A linear fit to the data shows a slope of -0.16 Bohr/a.u. over this range of light-matter coupling A_0, leading to an overall reduction in nuclear separation of roughly 0.15 Bohr. Even this relatively large amount would result in substantial changes to a local chemistry.

At this point, it is prudent to compare/benchmark the results of the DQMC for the polaritonic system with the state-of-the-art coupled cluster approach for polaritonic eigenstates, i.e., the self-consistent QED-CCSD method. This method encompasses diverse treatments of photonic excitation and
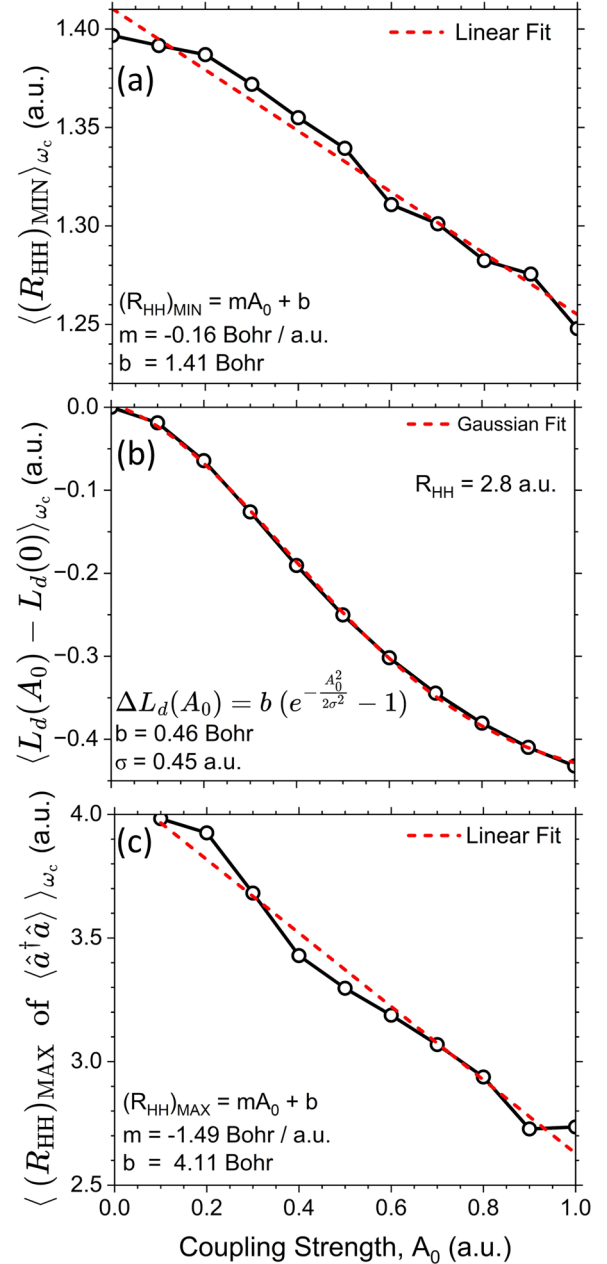

FIG. 3. (a) The location of the ground-state potential energy surface minimum, (b) the difference in wave-function localization, and (c) the location of the maximum photon number as a function of the light-matter coupling strength A_0. $\langle \cdots \rangle_{\omega_c}$ indicates an average over cavity frequencies $\omega_c = 5.0$, 10.0, 15.0, and 20.0 eV. Panels (a) and (c) are accompanied with a linear fit (red line), and panel (b) is shown with a Gaussian fit (red curve). In all cases, the data are interpolated with a cubic spline before locating the minimum or maximum of the function on a fine grid.

coupled excitations. In this work, the notation QED-CCSD-U2n-Sm specifies the level of the coupled cluster approach, where n represents the truncation level for the coupled photonic/electronic excitation and m indicates pure photonic excitation. As outlined in Refs. [30,45,86], multiple strategies can be applied; we focus on those where $n = m$ and $n \in \{1, 2\}$.
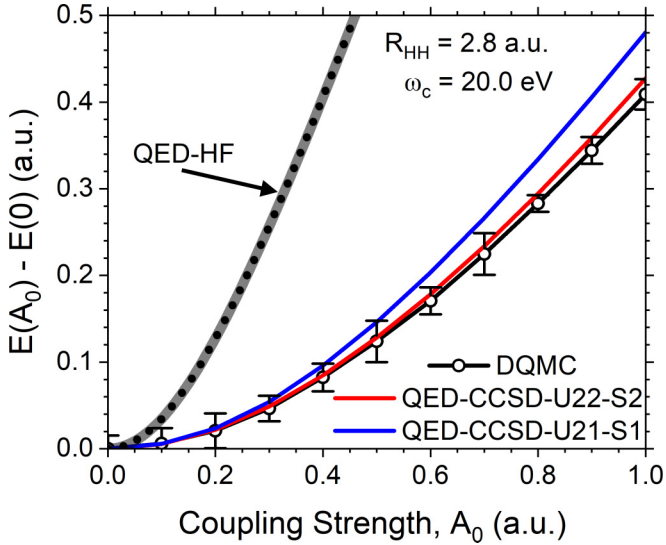
FIG. 4. The ground-state potential energy of the H_2 system as a function of light-matter coupling strength A_0. Four methods are compared: DQMC (current work, solid black curve and circles with error bars), QED-CCSD-U22-S2 (red curve, second lowest curve), QED-CCSD-U21-S1 (blue curve, third lowest curve), and QED-HF (dashed black and thick transparent black). The results of the QED-CCSD and QED-HF (thick transparent black) are computed using code published in Ref. [45], and the QED-HF (dotted black) is generated with an in-house code [30]. For the DQMC method, the error bars indicate the correlated standard deviation of the means. The cavity frequency and nuclear separation are fixed at $\omega_c = 20.0$ eV and $R_{HH} = 2.8$ a.u., respectively.

Figure 4 presents the results of these two approaches along with the DQMC of the current work as well as the QED-HF result. The change in the ground-state energy, $E(A_0) - E(0)$, of the polaritonic system as a function of the light-matter coupling strength A_0 is shown. The scQED-CCSD-U21-S1 approach includes only a single photonic excitation and its subsequent interaction with the electronic system. In contrast, the scQED-CCSD-U22-S2 approach includes double excitations of the cavity. This is expected to provide increased accuracy in a similar sense as the double electronic excitations increase the accuracy for the electronic ground state. First, the QED-HF results —generated from two different codes, Refs. [45] (thick transparent black) and [30] (dotted black), which are in mutual agreement with each other—significantly overestimate the change in ground-state energy with increasing light-matter coupling strength. The DQMC approach agrees well with the scQED-CCSD-U22-S2 approach up to roughly $A_0 \sim 0.5$ a.u., where the data points begin to diverge. However, all scQED-CCSD-U22-S2 results lie within the DQMC's correlated standard deviation. The scQED-CCSD-U21-S1 surpasses the DQMC's error bars around $A_0 \approx 0.4$ a.u. Given that the DQMC method captures exact correlations among electrons and between electrons and photons, we expect that a scQED-CCSD method with increased photonic excitation would align more closely with DQMC energies.

We next inspect the overlaps between the photonic wave function and the Fock state basis in the cavity position representation, $c_f(A_0) = \langle \phi_{ph}^{DQMC}(A_0) | f \rangle$, where f is the Fock

state with f photons, and $|\phi_{ph}^{DQMC}(A_0)\rangle$ is the wave function as computed by the DQMC approach in this study (see Figs. S4 and S5 in the supplemental material [83]). At $A_0 = 0.0$, 0.5, and 1.0 a.u., the amplitudes of the zero-photon Fock state are $c_f = 1.0$, 0.95, and 0.89, respectively. At $A_0 = 1.0$ a.u., there are significant contributions from the higher photon-number Fock states, c_f : 0.89($f = 0$), 0.37 ($f = 2$), 0.20 ($f = 4$), 0.12 ($f = 6$), and 0.07 ($f = 8$). It it worth noting that contributions from odd-photon-number Fock states are below 0.001, due to the "even"-symmetry of the ground-state wave function. Furthermore, over 99.5% of the photonic wave function is encapsulated by the first 10 Fock states ($0 \leqslant f \leqslant 9$) for $A_0 = 1.0$ a.u. This quantitative analysis of the photonic wave function underscores the necessity for the scQED-CCSD approach to incorporate additional photonic excitations to capture the required correlations. This also elucidates the discrepancy between the DQMC and scQED-CCSD results at large couplings.

It should be noted that utilizing unperturbed Fock/number states as the basis for photonic DOFs is a user choice. In principle, one may consider a polarized basis, such as the polarized Fock states [68] or the generalized coherent state basis [87]. These basis sets introduce a shift in the photonic coordinate potentially enabling a superior basis to the bare and unshifted Fock states presented in this work. Additionally, by nature of the coupled cluster approach, higher excitation levels than the explicitly included excitation operators are always present due to the exponential ansatz. For example, the authors of Ref. [45] utilized the shifted Fock basis [37] in the generation of the scQED-CCSD code used in this work. Thus the results shown in Fig. 4 should benefit from such transformation. Yet, some errors still exist due to the lack of a sufficiently large number of photonic excitations.

Here, we have shown that even the state-of-the-art coupled cluster approaches can be far from the exact solution even for simple systems such as H_2. We suggest the DQMC scheme as a valuable tool for gaining insights into elusive correlations within various systems, particularly when testing novel polaritonic many-body techniques.

Returning to the potential energy surface, Fig. S6 in the supplemental material [83] compares the potential energy surfaces in the cavity to the zero-coupling case, i.e., the differences represented as $E(A_0) - E(0)$. These quantities are shown across a range of light-matter coupling values for four distinct cavity frequencies: (a) 5.0, (b) 10.0, (c) 15.0, and (d) 20.0 eV. A noticeable maximum value emerges, especially in the case of large coupling. This maximum moves to shorter nuclear separation distances, R_{HH}, with increasing light-matter coupling strength. This observation resembles the shift noticed in the minima of the potential energy surface, and it will become apparent in the observables we discuss later in this study. In fact, all of these alterations are closely connected to modifications in the electronic wave function, specifically the molecular quadrupole, which is the focus of the upcoming section.

C. Polaritonic wave functions

Frequently, there is an interest in properties pertaining to the electronic part of the wave function confined within the
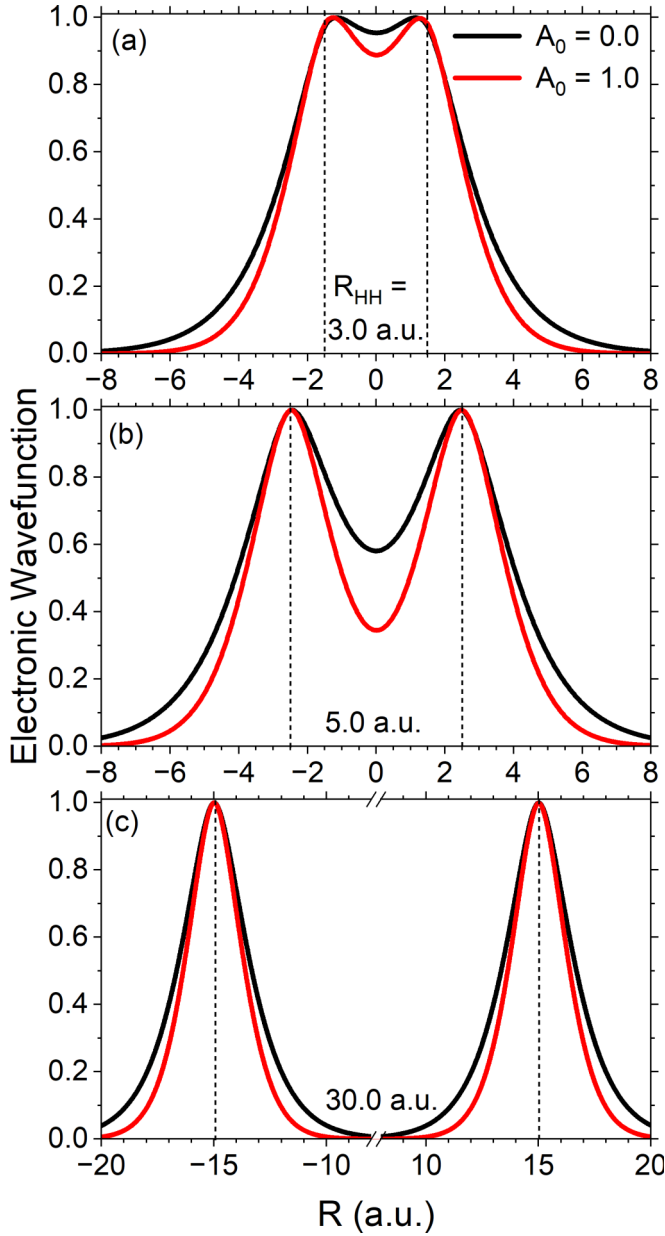
FIG. 5. The electronic wave function for the H_2 system coupled to the cavity at various nuclear separation lengths R_{HH} = 3 (a), 5 (b), and 30 (c) a.u. for two coupling strengths $A_0 = 0.0$ (black) and 0.5 (red, lower-in-magnitude curves) a.u. The wave functions are all normalized to unit by their maximum value for plotting purposes as $\phi_{el}^{DQMC}/\text{MAX}[\phi_{el}^{DQMC}] \to \phi_{el}^{DQMC}$. For all panels, the cavity frequency is set to $\omega_c = 20.0$ eV with cavity polarization being parallel to the bond axis.

cavity. The alterations noted within the electronic subsystem provide direct information regarding chemical reactions. The photonic wave function's expansion in the Fock basis has been previously illustrated in supplemental Figs. S4 and S5 [83]. Here we focus on the electronic wave function $|\phi_{el}^{DQMC}\rangle$ plotted in Fig. 5 at various nuclear separation lengths R_{HH}. For each nuclear separation, the wave functions for two distinct coupling strengths, $A_0 = 0.0$ and 0.5 a.u., are shown. A critical observation pertains to the influence of the cavity on
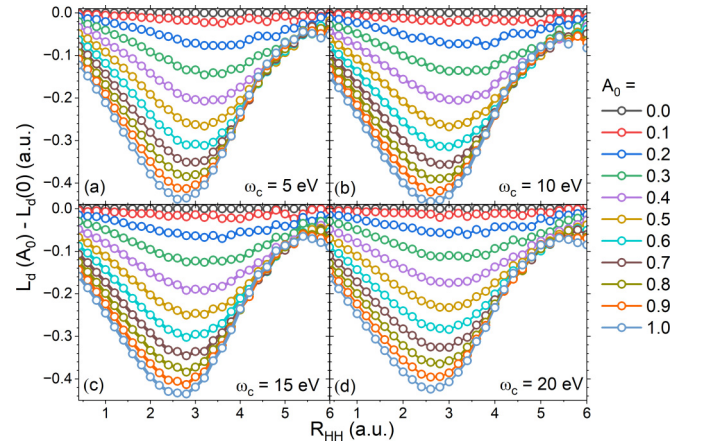

FIG. 6. The difference in wave-function localization of the ground state H_2 dissociation with respect to the pristine system (i.e., no cavity), $L_d(A_0) - L_d(0)$, at various coupling strengths A_0 from 0.0 to 1.0 a.u. in increments of 0.1 a.u. (colors, from top to bottom) for four cavity frequencies $\omega_c = 5.0$ (a), 10.0 (b), 15.0 (c), and 20.0 (d) eV.

the electronic wave function's localization. The underpinning for this behavior can be traced to the Pauli-Fierz Hamiltonian, which incorporates the molecular dipole operator via both direct light-matter interaction $\hat{H}_{el-ph}$ and through the DSE $\hat{H}_{DSE}$ term in Eq. (11). This implies that the wave function tends to become an eigenstate of the dipole (or position) operator, in the limit when $\hat{H}_{el-ph}, \hat{H}_{DSE} \gg \hat{H}_{el}$.

To characterize the localization in quantum-mechanical systems, the inverse participation ratio (IPR) is widely used as a quantitative metric [88–94]. The IPR assesses the spread of a quantum-mechanical wave function ψ across its basis. In the present case, the basis is continuous, real-space position R, or, more practically, discrete position R_j with uniform discretization $\Delta R = R_j - R_{j-1}$ and is defined as

$$\text{IPR} = \frac{1}{\sum_j P_j^2}, \qquad P_j = \frac{|\psi(R_j)|^2}{\sum_k |\psi(R_k)|^2},$$

$$\text{IPR} = \frac{1}{\int \frac{dR}{\Delta R} P(R)^2}, \qquad P(R) = \frac{|\psi(R)|^2}{\int \frac{dR}{\Delta R} |\psi(R)|^2} \qquad (23)$$

for each representation, respectively. Here, $|\psi(R_j)| = \psi(R_j) \equiv \phi_{el}^{DQMC}(R_j)$ in this work, since the wave function in the position representation is both real- and positive-valued. The resulting IPR (an integer) spans a range between 1 and N_{basis}, where N_{basis} is the number of basis states (or discrete positions R_j). When $\psi(R_j) = \delta_{R_j,R_0}$, IPR = 1, and when $\psi(R_j) = 1/N_{basis}$, IPR = N_{basis}. To convert this value into a spatial length, one can multiply by the grid spacing ΔR to obtain the localization length $L_d = \text{IPR} \times \Delta R$.

Supplemental Fig. S7 [83] displays the computed localization length, L_d, for every DQMC simulation of the electronic wave function, projected along the bond axis. The most meaningful representation is rather the change in the localization with respect to outside the cavity, $L_d(A_0) - L_d(0)$, which is presented in Fig. 6 for all light-matter coupling strengths A_0 and four cavity frequencies ω_c. There is a pronounced nuclear separation R_{HH} where the localization of the wave function

exhibits a maximal change compared to outside the cavity, which strongly depends on the light-matter coupling A_0. This trend mirrors our earlier observations regarding the potential energy surface minimum, as depicted in Fig. 3(a). The cavity frequency, again, has a minimal effect on the localization of the electronic wave function.

At a fixed nuclear separation of $R_{HH} = 2.8$ a.u. (near the maximum localization), the extent of enhanced wave-function localization is presented in Fig. 3(b) and follows a Gaussian function of the coupling strength. The data shown in Fig. 3(b) represent an average over four cavity frequencies, which provide increased statistical clarity. Our results are suggestive of a generic trend, wherein the electronic localization adheres to a Gaussian profile as a function of the coupling strength. Such Gaussian correlations with coupling strength have also been observed in relation to the splitting between ground and excited state avoided crossings for the LiF system [68]. These were attributed to a wave-function overlap between two shifted Fock states (i.e., a Gaussian involving the light-matter coupling strength) in the polarized Fock state representation.

D. Average photon number

The final observable of interest is the average photon number in the ground state. This is a direct extension of our earlier discussion about the overlap of the DQMC photonic wave function with the number (or Fock) basis (see supplemental Figs. S4 and S5 [83]). In the photon number basis, the expression $\langle \hat{a}^\dagger \hat{a} \rangle$ represents the average occupation of the mode in the Pauli-Fierz (or length) gauge, which may differ from that in the Coulomb (or "p · A") gauge. Nevertheless, the average occupation can undergo a unitary rotation to any other gauge [28,95], and we expect that the absolute magnitudes of the photon number might differ, but the physical trends should remain unchanged.

Figures 7(a)–7(d) present the average photon number $\langle \hat{a}^\dagger \hat{a} \rangle$ throughout the H_2 dissociation, for various light-matter coupling strengths A_0 and for four cavity frequencies ω_c. Analogous to the previous observables, such as the change in electronic wave-function localization L_d, there is a distinct peak in photon number at a certain value of R_{HH}, depending on the coupling strength A_0. The peak's location is illustrated in Fig. 3(c) and fit to a linear function, where the data have been averaged over the four cavity frequencies ω_c.

At a fixed $R_{HH} = 2.8$ a.u., as depicted in Fig. 7(e), the average photon number behaves intriguingly. For smaller light-matter coupling strengths $A_0 \leqslant 0.5$ a.u., the photon number increases quadratically, $\langle \hat{a}^\dagger \hat{a} \rangle \sim \omega_c A_0^2$, with its leading coefficient dependent on the cavity frequency. Conversely, for larger light-matter coupling $A_0 \geqslant 0.5$ a.u., the average photon number increases linearly (up to the maximal coupling strength computed in this work) with slopes dependent on the cavity frequency, $\langle \hat{a}^\dagger \hat{a} \rangle \sim \omega_c A_0$. The convergence of the average photon number in the ground state is tested with respect to the simulation time step, as shown in supplemental Fig. S8 [83]. Given these substantial changes in the photon number, there exists a potential for fascinating quantum measurements in highly entangled many-body states, especially in dynamic scenarios where complex interplay between the
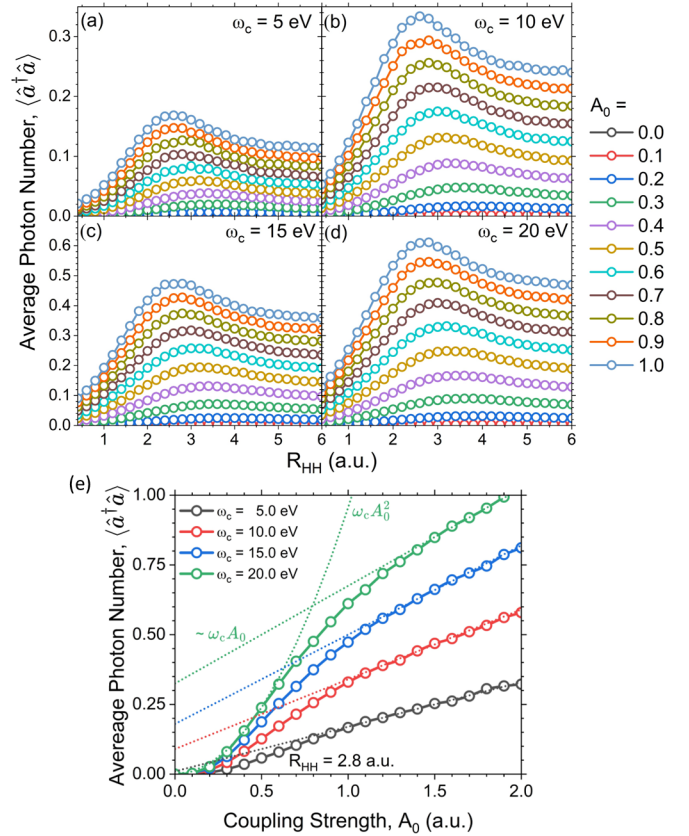

FIG. 7. The average photon number, $\langle \hat{a}^\dagger \hat{a} \rangle$, throughout the ground-state H_2 dissociation with respect to the uncoupled system, $L_d(A_0) - L_d(0)$, at various coupling strengths A_0 from 0.0 to 1.0 a.u. in increments of 0.1 a.u. (colors, bottom to top) for four cavity frequencies $\omega_c = 5.0$ (a), 10.0 (b), 15.0 (c), and 20.0 (d) eV. (e) The average photon number, $\langle \hat{a}^\dagger \hat{a} \rangle$, as a function of light-matter coupling strength A_0 for a fixed nuclear separation $R_{HH} = 2.8$ a.u. for four cavity frequencies $\omega_c = 5.0$ (black, bottom), 10.0 (red, lower middle), 15.0 (blue, upper middle), and 20.0 (green, top) eV. The dotted curves present the scaling at the low (i.e., quadratic) and high (i.e., linear) coupling regimes.

nuclear and photonic DOFs can induce significant fluctuations in the photon number, even in the ground polaritonic state.

E. Linear infrared spectroscopy

The infrared spectrum of the H_2 system is not experimentally accessible due to the lack of ground-state electronic dipole moment, $\langle \phi_0(R_{HH})|\hat{\mu}|\phi_0(R_{HH})\rangle = 0$, for all R_{HH} due to the molecular symmetry. However, we can still extract meaningful spectroscopic quantities whose trends can be generalized to more complicated molecular systems. The simplest quantity is the vibronic transition frequency. The vibrational frequency was computed using two approaches: The discrete variable representation (DVR) [96] and the harmonic mode approximation (HMA). See the supplemental material [83] for details on the DVR and HMA. The DVR approach is the most rigorous and is expected to be less sensitive to the statistical error present in the DQMC simulations. This approach also exactly captures the anharmonicity of the ground-state potential energy surface. Contrary to this, the HMA (which
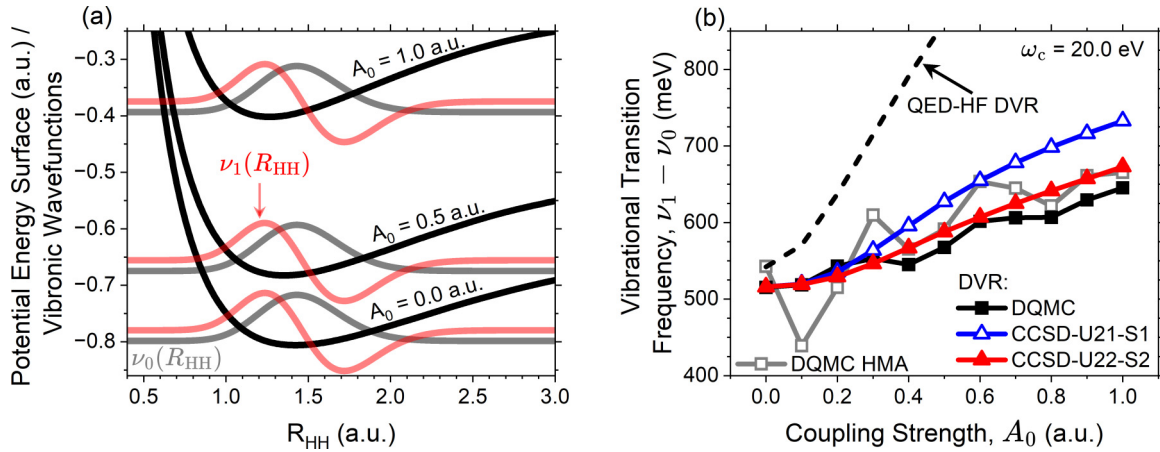
FIG. 8. (a) The potential energy surface (solid black) and first two vibronic wave functions (ν_0 gray, ν_1 red) are shown for three light-matter coupling strengths $A_0 = 0.0, 0.5$, and 1.0 a.u. (b) The principal vibrational transition frequency, $\nu_1 - \nu_0$, of the H_2 system is shown as a function of the light-matter coupling strength A_0. Four polaritonic structure methods are shown using the DVR approach: DQMC (black filled squares), QED-Hartree-Fock (black dashed), CCSD-U21-S1 (blue filled triangles), and CCSD-U22-S2 (red open triangles). Further, the HMA is shown for the DQMC approach (gray open squares). All data are computed with cavity frequency $\omega_c = 20.0$ eV.

is ubiquitously used in electronic structure theory) is highly sensitive to the accuracy of the ground-state energy with respect to the nuclear displacement. Due to this, we expect larger errors to be present in the HMA DQMC approach since the ground-state energy exhibits finite statistical fluctuations (see the error bars in Fig. 4). These statistical errors will also arise when computing other observables that depend on numerical finite differences of the energy, such as the forces on the nuclei, $\mathbf{F} = -\langle \phi_0(\mathbf{R}) | \nabla_{\mathbf{R}} \hat{H} | \phi_0(\mathbf{R}) \rangle$, of a molecular system [97].

The potential energy surface (solid black) and the first two vibronic wave functions (ν_0 gray, ν_1 red) are shown in Fig. 8(a) for three light-matter coupling strengths $A_0 = 0.0$, 0.5, and 1.0 a.u. The computed principle vibrational transition frequency, $\nu_1 - \nu_0$, of the H_2 system is depicted in Fig. 8(b) as a function of the light-matter coupling strength A_0. Here, we present results obtained using four polaritonic structure methods employing the DVR approach, including DQMC (black filled squares), QED-HF (black dashed), CCSD-U21-S1 (blue filled triangles), and CCSD-U22-S2 (red open triangles). Additionally, the HMA is depicted for the DQMC approach (gray open squares). All data are computed with cavity frequency $\omega_c = 20.0$ eV.

The trends of the vibrational transition frequency closely resemble those of the ground-state energy itself (Fig. 4). At zero light-matter coupling $A_0 = 0.0$ a.u., both the CC and DQMC approaches agree on the vibrational transition frequency. The HF result is slightly blueshifted in this comparison. With increasing coupling strength, the vibrational transition frequency is expected to increase, since the electronic wave functions undergo a strong localization (see Fig. 4) and hence are expected to produce a narrower potential energy surface. As in the case of the ground-state energy itself (see Fig. 4), with increasing coupling strength, the HF approach overestimates the cavity effects. The DQMC approach suggests the weakest effects, followed by the CCSD-U22-S2 and CCSD-U21-S1 methods. These results imply that the presence of stronger electron-electron and electron-photon

correlations reduces the overall effects of the cavity on the nuclear vibrational frequency shift. We expect these trends in vibrational frequencies to generalize to more complicated molecules where the infrared spectrum can be measured and analyzed. Such molecules and their vibrational spectra will be the subject of our future work.

As a final note, the statistical error in the numerical derivative of the nuclear positions is evidenced by the DQMC HMA (gray open squares). While the overall trend of the cavity effects is clearly present, the large fluctuations between data points suggest that the DQMC approach is very sensitive to the evaluation of numerical gradients, which is a well-known issue of DQMC approaches [97].

IV. CONCLUSIONS

In summary, this work presents a diffusion quantum Monte Carlo (DQMC) scheme for direct simulations of molecular polaritons, which necessarily includes complicated correlations between the electronic, nuclear, and photonic degrees of freedom. This scheme represents a thoroughly *ab initio* approach, which provides the exact solution to any two-electron system interacting with, in principle, infinite cavity modes. As a testament to its capabilities, we study the H_2 molecular dissociation coupled to a single cavity mode. The results are compared directly with state-of-the-art quantum electrodynamic (QED) coupled cluster approaches, which provides an exact solution to the pristine molecular system (in the absence of cavity) in the infinite basis limit . We emphasize that the accuracy of the latter method is largely contingent upon the truncation of photonic excitation in the exponential ansatz. Our comparative analysis shows that even the highest fidelity approach currently available fails in even the simplest molecular system when the light-matter coupling strengths become large enough to necessarily include contributions from photonic excitations beyond one or two photonic number (or Fock) states.

The DQMC approach is then used to explore various observables for the H_2 system, such as the localization extent

of the electronic and the decomposition of the photonic wave functions in the Fock basis. Additionally, linear trends in the light-matter coupling strength are identified for the nuclear separations, which exhibit (I) the minimum of the potential energy surfaces, and (II) the maximum average photon number. Moreover, a Gaussian trend emerges in the changes related to wave-function localization. In the former two cases, the change of the properties with respect to the nuclear separation length are directly relevant to modifications of chemical reactions, where even the smallest nuclear displacement may alter reaction pathways and resulting products. Meanwhile, the wave function's localization can offer insights into processes demanding wave-function overlap, such as Dexter energy transfer or H/J-aggregates representing excitonic systems. This holds implications for exciton-polariton transport in molecular and solid-state materials.

Altogether, DQMC represents a promising route toward the direct and accurate simulation of simple systems, where the results are exact. Applications to more intricate systems are possible as well by leveraging the fixed node approximation for many-electron systems and excited states [70,98–100]. We note that in the realm of polaritonic DQMC, the fixed node approximation needs to be carefully implemented, since the nodal surface will likely undergo changes as a result of interaction with the cavity. Thus, using a mean-field wave function (i.e., Hartree-Fock) one must either (I) include the cavity effects on the single-particle orbitals (i.e., QED-HF) [52] or (II) allow the nodal surface to relax in order to minimize the energy while retaining the correct electronic statistics. This can be introduced via an importance-sampling algorithm [76], which adds an effective drift term to the Gaussian random steps encoded with information regarding the provided reference wave function. It is important to note that the extension of the present polaritonic DQMC approach, specifically including the photonic DOF, will not impact an incorporation of an importance-sampling algorithm into polaritonic DQMC, so long as the trial or reference wave function accurately captures the nodal structure of the system. These ideas direct our future studies in this area.

The presented DQMC approach can be further readily employed to explore polaron formation and its inherent properties, including polaron radius and binding energy, given the bosonic nature of both photons and phonons. Most importantly, and without loss of accuracy, the many-molecule and many-cavity-mode systems can be directly simulated, assuming (I) the molecules do not interact directly via Coulomb potential (i.e., only through mutual interaction with the cavity) and (II) the cavity modes do not include the complex-valued nature of the Pauli-Fierz Hamiltonian in the absence of the long-wavelength approximation. Despite these constraints, our approach illuminates solutions for simple molecular systems inside the cavity. Further, the extension toward plasmonic cavities, where the light-matter coupling strength depends on position, $A_0 \rightarrow A_0(\mathbf{r})$, would be straightforward with minimal changes to the code. DQMC's relative simplicity and favorable scaling with dimensionality, typically a constraint for advanced methods like coupled cluster, cements its place as a promising tool for investigating *ab initio* molecular systems inside cavities.

[1] K. Nagarajan, A. Thomas, and T. W. Ebbesen, Chemistry under vibrational strong coupling, J. Am. Chem. Soc. **143**, 16877 (2021).

[2] F. J. Garcia-Vidal, C. Ciuti, and T. W. Ebbesen, Manipulating matter by strong coupling to vacuum fields, Science **373**, eabd0336 (2021).

[3] J. A. Hutchison, T. Schwartz, C. Genet, E. Devaux, and T. W. Ebbesen, Modifying chemical landscapes by coupling to vacuum fields, Angew. Chem. Int. Ed. **51**, 1592 (2012).

[4] T. Schwartz, J. A. Hutchison, C. Genet, and T. W. Ebbesen, Reversible switching of ultrastrong light-molecule coupling, Phys. Rev. Lett. **106**, 196405 (2011).

[5] T. W. Ebbesen, Hybrid light–matter states in a molecular and material science perspective, Acc. Chem. Res. **49**, 2403 (2016).

[6] A. Sau, K. Nagarajan, B. Patrahau, L. Lethuillier-Karl, R. M. A. Vergauwe, A. Thomas, J. Moran, C. Genet, and T. W. Ebbesen, Modifying Woodward–Hoffmann stereoselectivity under vibrational strong coupling, Angew. Chem. Int. Ed. **60**, 5712 (2021).

[7] A. Thomas, L. Lethuillier-Karl, K. Nagarajan, R. M. A. Vergauwe, J. George, T. Chervy, A. Shalabney, E. Devaux, C. Genet, J. Moran, and T. W. Ebbesen, Tilting a ground-state reactivity landscape by vibrational strong coupling, Science **363**, 615 (2019).

[8] A. Thomas, J. George, A. Shalabney, M. Dryzhakov, S. J. Varma, J. Moran, T. Chervy, X. Zhong, E. Devaux, C. Genet, J. A. Hutchison, and T. W. Ebbesen, Ground-state chemical reactivity under vibrational coupling to the vacuum electromagnetic field, Angew. Chem. Int. Ed. **55**, 11462 (2016).

[9] A. Thomas, A. Jayachandran, L. Lethuillier-Karl, R. M. A. Vergauwe, K. Nagarajan, E. Devaux, C. Genet, J. Moran, and T. W. Ebbesen, Ground state chemistry under vibrational

strong coupling: dependence of thermodynamic parameters on the Rabi splitting energy, Nanophotonics **9**, 249 (2020).

[10] J. Lather, P. Bhatt, A. Thomas, T. W. Ebbesen, and J. George, Cavity catalysis by cooperative vibrational strong coupling of reactant and solvent molecules, Angew. Chem. Int. Ed. **58**, 10635 (2019).

[11] K. Hirai, J. A. Hutchison, and H. Uji-i, Molecular chemistry in cavity strong coupling, Chem. Rev. **123**, 8099 (2023).

[12] B. S. Simpkins, A. D. Dunkelberger, and I. Vurgaftman, Control, modulation, and analytical descriptions of vibrational strong coupling, Chem. Rev. **123**, 5020 (2023).

[13] A. Thomas, E. Devaux, K. Nagarajan, G. Rogez, M. Seidel, F. Richard, C. Genet, M. Drillon, and T. W. Ebbesen, Large enhancement of ferromagnetism under a collective strong coupling of YBCO nanoparticles, Nano Lett. **21**, 4365 (2021).

[14] R. M. A. Vergauwe, A. Thomas, K. Nagarajan, A. Shalabney, J. George, T. Chervy, M. Seidel, E. Devaux, V. Torbeev, and T. W. Ebbesen, Modification of enzyme activity by vibrational strong coupling of water, Angew. Chem. Int. Ed. **58**, 15324 (2019).

[15] A. M. Berghuis, V. Serpenti, M. Ramezani, S. Wang, and J. G. Rivas, Light–matter coupling strength controlled by the orientation of organic crystals in plasmonic cavities, J. Phys. Chem. C **124**, 12030 (2020).

[16] A. M. Berghuis, R. H. Tichauer, L. M. A. de Jong, I. Sokolovskii, P. Bai, M. Ramezani, S. Murai, G. Groenhof, and J. G. Rivas, Controlling exciton propagation in organic crystals through strong coupling to plasmonic nanoparticle arrays, ACS Photon. **9**, 2263 (2022).

[17] D. Xu, A. Mandal, J. M. Baxter, S.-W. Cheng, I. Lee, H. Su, S. Liu, D. R. Reichman, and M. Delor, Ultrafast imaging of polariton propagation and interactions, Nat. Commun. **14**, 3881 (2023).

[18] H. Deng, H. Haug, and Y. Yamamoto, Exciton-polariton Bose-Einstein condensation, Rev. Mod. Phys. **82**, 1489 (2010).

[19] G. G. Rozenman, K. Akulov, A. Golombek, and T. Schwartz, Long-range transport of organic exciton-polaritons revealed by ultrafast microscopy, ACS Photon. **5**, 105 (2018).

[20] J. M. Lüttgens, F. J. Berger, and J. Zaumseil, Population of exciton–polaritons via luminescent sp^3 defects in single-walled carbon nanotubes, ACS Photon. **8**, 182 (2021).

[21] C. Möhl, A. Graf, F. J. Berger, J. Lüttgens, Y. Zakharko, V. Lumsargis, M. C. Gather, and J. Zaumseil, Trion-polariton formation in single-walled carbon nanotube microcavities, ACS Photon. **5**, 2074 (2018).

[22] A. Graf, L. Tropf, Y. Zakharko, J. Zaumseil, and M. C. Gather, Near-infrared exciton-polaritons in strongly coupled single-walled carbon nanotube microcavities, Nat. Commun. **7**, 13078 (2016).

[23] A. Graf, M. Held, Y. Zakharko, L. Tropf, M. C. Gather, and J. Zaumseil, Electrical pumping and tuning of exciton-polaritons in carbon nanotube microcavities, Nat. Mater. **16**, 911 (2017).

[24] M. Son, Z. T. Armstrong, R. T. Allen, A. Dhavamani, M. S. Arnold, and M. T. Zanni, Energy cascades in donor-acceptor exciton-polaritons observed by ultrafast two-dimensional white-light spectroscopy, Nat. Commun. **13**, 7305 (2022).

[25] R. T. Allen, A. Dhavamani, M. Son, S. Kéna-Cohen, M. T. Zanni, and M. S. Arnold, Population of subradiant states in carbon nanotube microcavities in the ultrastrong light–matter coupling regime, J. Phys. Chem. C **126**, 8417 (2022).

[26] A. Mandal, D. Xu, A. Mahajan, J. Lee, M. Delor, and D. R. Reichman, Microscopic theory of multimode polariton dispersion in multilayered materials, Nano Lett. **23**, 4082 (2023).

[27] L. P. Lindoy, A. Mandal, and D. R. Reichman, Resonant cavity modification of ground-state chemical kinetics, J. Phys. Chem. Lett. **13**, 6580 (2022).

[28] A. Mandal, M. A. D. Taylor, B. M. Weight, E. R. Koessler, X. Li, and P. Huo, Theoretical advances in polariton chemistry and molecular cavity quantum electrodynamics, Chem. Rev. **123**, 9786 (2023).

[29] M. Ruggenthaler, D. Sidler, and A. Rubio, Understanding polaritonic chemistry from *Ab Initio* quantum electrodynamics, Chem. Rev. **123**, 11191 (2023).

[30] B. M. Weight, X. Li, and Y. Zhang, Theory and modeling of light-matter interactions in chemistry: current and future, Phys. Chem. Chem. Phys. **25**, 31554 (2023).

[31] D. S. Wang and S. F. Yelin, A roadmap toward the theory of vibrational polariton chemistry, ACS Photon. **8**, 2818 (2021).

[32] T. S. Haugland, J. P. Philbin, T. K. Ghosh, M. Chen, H. Koch, and P. Narang, Understanding the polaritonic ground state in cavity quantum electrodynamics, arXiv:2307.14822.

[33] J. J. Foley IV, J. F. McTague, and A. E. DePrince III, *Ab initio* methods for polariton chemistry, Chem. Phys. Rev. **4**, 041301 (2023).

[34] J. Flick, H. Appel, M. Ruggenthaler, and A. Rubio, Cavity Born–Oppenheimer approximation for correlated electron–nuclear-photon systems, J. Chem. Theory Comput. **13**, 1616 (2017).

[35] T. Schnappinger, D. Sidler, M. Ruggenthaler, A. Rubio, and M. Kowalewski, Cavity-Born-Oppenheimer Hartree-Fock ansatz: Light-matter properties of strongly coupled molecular ensembles, J. Phys. Chem. Lett. **14**, 8024 (2023).

[36] B. M. Weight, T. D. Krauss, and P. Huo, Investigating molecular exciton polaritons using *Ab Initio* cavity quantum electrodynamics, J. Phys. Chem. Lett. **14**, 5901 (2023).

[37] T. S. Haugland, E. Ronca, E. F. Kjønstad, A. Rubio, and H. Koch, Coupled cluster theory for molecular polaritons: Changing ground and excited states, Phys. Rev. X **10**, 041043 (2020).

[38] X. Li and Y. Zhang, First-principles molecular quantum electrodynamics theory at all coupling strengths, arXiv:2310.18228.

[39] J. Flick, C. Schäfer, M. Ruggenthaler, H. Appel, and A. Rubio, *Ab initio* optimized effective potentials for real molecules in optical cavities: Photon contributions to the molecular ground state, ACS Photon. **5**, 992 (2018).

[40] C. Pellegrini, J. Flick, I. V. Tokatly, H. Appel, and A. Rubio, Optimized effective potential for quantum electrodynamical time-dependent density functional theory, Phys. Rev. Lett. **115**, 093001 (2015).

[41] J. Flick, N. Rivera, and P. Narang, Strong light-matter coupling in quantum chemistry and quantum photonics, Nanophotonics **7**, 1479 (2018).

[42] M. Ruggenthaler, J. Flick, C. Pellegrini, H. Appel, I. V. Tokatly, and A. Rubio, Quantum-electrodynamical density-functional theory: Bridging quantum optics and electronic-structure theory, Phys. Rev. A **90**, 012508 (2014).

[43] M. Ruggenthaler, N. Tancogne-Dejean, J. Flick, H. Appel, and A. Rubio, From a quantum-electrodynamical light–matter description to novel spectroscopies, Nat. Rev. Chem. **2**, 1 (2018).

[44] T. S. Haugland, C. Schäfer, E. Ronca, A. Rubio, and H. Koch, Intermolecular interactions in optical cavities: An *ab initio* QED study, J. Chem. Phys. **154**, 094113 (2021).

[45] F. Pavošević, S. Hammes-Schiffer, A. Rubio, and J. Flick, Cavity-modulated proton transfer reactions, J. Am. Chem. Soc. **144**, 4995 (2022).

[46] A. E. DePrince, Cavity-modulated ionization potentials and electron affinities from quantum electrodynamics coupled-cluster theory, J. Chem. Phys. **154**, 094112 (2021).

[47] Z.-H. Cui, A. Mandal, and D. R. Reichman, Variational Lang-Firsov approach plus Møller-Plesset perturbation theory with applications to *ab initio* polariton chemistry, J. Chem. Theory Comput. **20**, 1143 (2024).

[48] J. Flick and P. Narang, *Ab initio* polaritonic potential-energy surfaces for excited-state nanophotonics and polaritonic chemistry, J. Chem. Phys. **153**, 094116 (2020).

[49] J. Yang, Q. Ou, Z. Pei, H. Wang, B. Weng, Z. Shuai, K. Mullen, and Y. Shao, Quantum-electrodynamical time-dependent density functional theory within Gaussian atomic basis, J. Chem. Phys. **155**, 064107 (2021).

[50] J. Yang, Z. Pei, E. C. Leon, C. Wickizer, B. Weng, Y. Mao, Q. Ou, and Y. Shao, Cavity quantum-electrodynamical time-dependent density functional theory within Gaussian atomic basis. II. Analytic energy gradient, J. Chem. Phys. **156**, 124104 (2022).

[51] M. D. Liebenthal, N. Vu, and A. E. DePrince, Equation-of-motion cavity quantum electrodynamics coupled-cluster theory for electron attachment, J. Chem. Phys. **156**, 054105 (2022).

[52] M. D. Liebenthal, N. Vu, and A. E. DePrince III, Assessing the effects of orbital relaxation and the coherent-state transformation in quantum electrodynamics density functional and coupled-cluster theories, J. Phys. Chem. A **127**, 5264 (2023).

[53] N. Vu, G. M. McLeod, K. Hanson, and A. E. DePrince, Enhanced diastereocontrol via strong light–matter interactions in an optical cavity, J. Phys. Chem. A **126**, 9303 (2022).

[54] U. Mordovina, C. Bungey, H. Appel, P. J. Knowles, A. Rubio, and F. R. Manby, Polaritonic coupled-cluster theory, Phys. Rev. Res. **2**, 023262 (2020).

[55] N. Vu, D. Mejia-Rodriguez, N. Bauman, A. Panyala, E. Mutlu, N. Govind, and J. Foley, Cavity quantum electrodynamics complete active space configuration interaction theory, J. Chem. Theory Comput. **20**, 1214 (2024).

[56] J. Flick and P. Narang, Cavity-correlated electron-nuclear dynamics from first principles, Phys. Rev. Lett. **121**, 113002 (2018).

[57] C. Schäfer, F. Buchholz, M. Penz, M. Ruggenthaler, and A. Rubio, Making *ab initio* QED functional(s): Nonperturbative and photon-free effective frameworks for strong light–matter coupling, Proc. Natl. Acad. Sci. USA **118**, e2110464118 (2021).

[58] J. Flick, Simple exchange-correlation energy functionals for strongly coupled light-matter systems based on the fluctuation-dissipation theorem, Phys. Rev. Lett. **129**, 143201 (2022).

[59] G. M. Akselrod, J. Huang, T. B. Hoang, P. T. Bowen, L. Su, D. R. Smith, and M. H. Mikkelsen, Large-area metasurface perfect absorbers from visible to near-infrared, Adv. Mater. **27**, 8028 (2015).

[60] T. B. Hoang, G. M. Akselrod, and M. H. Mikkelsen, Ultrafast room-temperature single photon emission from quantum dots coupled to plasmonic nanocavities, Nano Lett. **16**, 270 (2016).

[61] H. Zeng, J. B. Pérez-Sánchez, C. T. Eckdahl, P. Liu, W. J. Chang, E. A. Weiss, J. A. Kalow, J. Yuen-Zhou, and N. P. Stern, Control of photoswitching kinetics with strong light–matter coupling in a cavity, J. Am. Chem. Soc. **145**, 19655 (2023).

[62] L. Qiu, A. Mandal, O. Morshed, M. T. Meidenbauer, W. Girten, P. Huo, A. N. Vamivakas, and T. D. Krauss, Molecular polaritons generated from strong coupling between CdSe nanoplatelets and a dielectric optical cavity, J. Phys. Chem. Lett. **12**, 5030 (2021).

[63] R. Bhuyan, J. Mony, O. Kotov, G. W. Castellanos, J. Gómez Rivas, T. O. Shegai, and K. Börjesson, The rise and current status of polaritonic photochemistry and photophysics, Chem. Rev. **123**, 10877 (2023).

[64] M. R. Bourgeois, E. K. Beutler, S. Khorasani, N. Panek, and D. J. Masiello, Nanometer-scale spatial and spectral mapping of exciton polaritons in structured plasmonic cavities, Phys. Rev. Lett. **128**, 197401 (2022).

[65] J. Guan, J.-E. Park, S. Deng, M. J. H. Tan, J. Hu, and T. W. Odom, Light–matter interactions in hybrid material metasurfaces, Chem. Rev. **122**, 15177 (2022).

[66] F. Pavošević, R. L. Smith, and A. Rubio, Computational study on the catalytic control of endo/exo Diels-Alder reactions by cavity quantum vacuum fluctuations, Nat. Commun. **14**, 2766 (2023).

[67] F. Pavosevic, R. L. Smith, and A. Rubio, Cavity click chemistry: Cavity-catalyzed azide-alkyne cycloaddition, J. Phys. Chem. A **127**, 10184 (2023).

[68] A. Mandal, S. M. Vega, and P. Huo, Polarized fock states and the dynamical Casimir effect in molecular cavity quantum electrodynamics, J. Phys. Chem. Lett. **11**, 9215 (2020).

[69] N. Metropolis and S. Ulam, The Monte Carlo method, J. Am. Stat. Assoc. **44**, 335 (1949).

[70] W. M. C. Foulkes, L. Mitas, R. J. Needs, and G. Rajagopal, Quantum Monte Carlo simulations of solids, Rev. Mod. Phys. **73**, 33 (2001).

[71] J. Thijssen, *Computational Physics* (Cambridge University Press, Cambridge, 2007).

[72] R. M. Martin, L. Reining, and D. M. Ceperley, *Interacting Electrons* (Cambridge University Press, Cambridge, 2016).

[73] J. R. Johansson, P. D. Nation, and F. Nori, QuTiP: An open-source Python framework for the dynamics of open quantum systems, Comput. Phys. Commun. **183**, 1760 (2012).

[74] J. R. Johansson, P. D. Nation, and F. Nori, QuTiP 2: A Python framework for the dynamics of open quantum systems, Comput. Phys. Commun. **184**, 1234 (2013).

[75] G. M. Longo, C. M. Coppola, D. Giordano, and S. Longo, The unbiased diffusion Monte Carlo: a versatile tool for two-electron systems confined in different geometries, Eur. Phys. J. D **75**, 83 (2021).

[76] C. J. Umrigar, M. P. Nightingale, and K. J. Runge, A diffusion Monte Carlo algorithm with very small time-step errors, J. Chem. Phys. **99**, 2865 (1993).

[77] R. Assaraf, M. Caffarel, and A. Khelif, Diffusion Monte Carlo methods with a fixed number of walkers, Phys. Rev. E **61**, 4566 (2000).

[78] H. F. Trotter, On the product of semi-groups of operators, Proc. Am. Math. Soc. USA **10**, 545 (1959).

[79] M. Suzuki, Fractal decomposition of exponential operators with applications to many-body theories and Monte Carlo simulations, Phys. Lett. A **146**, 319 (1990).

[80] H. Flyvbjerg and H. G. Petersen, Error estimates on averages of correlated data, J. Chem. Phys. **91**, 461 (1989).

[81] U. Wolff, Monte Carlo errors with less errors, Comput. Phys. Commun. **156**, 143 (2004).

[82] M. Jonsson, Standard error estimation by an automated blocking method, Phys. Rev. E **98**, 043304 (2018).

[83] See Supplemental Material at http://link.aps.org/supplemental/10.1103/PhysRevA.109.032804 for additional figures which aid the discussion in the main text, including Fock/number state projections for the photonic wave function, differences in polaritonic potential energy surfaces, localization lengths of the electronic wave function, and the time-step convergence of the average photon number. Our implementation is publicly available on GitHub: https://github.com/bradenmweight/QuantumMonteCarlo

[84] Q. Sun, T. C. Berkelbach, N. S. Blunt, G. H. Booth, S. Guo, Z. Li, J. Liu, J. D. McClain, E. R. Sayfutyarova, S. Sharma, S. Wouters, and G. K.-L. Chan, PySCF: the Python-based simulations of chemistry framework, WIREs Computat. Molec. Sci. **8**, e1340 (2018).

[85] Q. Sun, X. Zhang, S. Banerjee, P. Bao, M. Barbry, N. S. Blunt, N. A. Bogdanov, G. H. Booth, J. Chen, Z.-H. Cui, J. J. Eriksen, Y. Gao, S. Guo, J. Hermann, M. R. Hermes, K. Koh, P. Koval, S. Lehtola, Z. Li, J. Liu *et al.*, Recent developments in the PySCF program package, J. Chem. Phys. **153**, 024109 (2020).

[86] A. F. White, Y. Gao, A. J. Minnich, and G. K.-L. Chan, A coupled cluster framework for electrons and phonons, J. Chem. Phys. **153**, 224112 (2020).

[87] T. G. Philbin, Generalized coherent states, Am. J. Phys. **82**, 742 (2014).

[88] S. Tretiak and S. Mukamel, Density matrix analysis and simulation of electronic excitations in conjugated and aggregated molecules, Chem. Rev. **102**, 3171 (2002).

[89] B. M. Weight, B. J. Gifford, S. Tretiak, and S. Kilina, Interplay between electrostatic properties of molecular adducts and their positions at carbon nanotubes, J. Phys. Chem. C **125**, 4785 (2021).

[90] S. Kilina, E. R. Batista, P. Yang, S. Tretiak, A. Saxena, R. L. Martin, and D. L. Smith, Electronic structure of self-assembled amorphous polyfluorenes, ACS Nano **2**, 1381 (2008).

[91] B. M. Weight, M. Zheng, and S. Tretiak, Signatures of chemical dopants in simulated resonance Raman spectroscopy of carbon nanotubes, J. Phys. Chem. Lett. **14**, 1182 (2023).

[92] Y. Zheng, B. M. Weight, A. C. Jones, V. Chandrasekaran, B. J. Gifford, S. Tretiak, S. K. Doorn, and H. Htoon, Photoluminescence dynamics defined by exciton trapping potential of coupled defect states in DNA-functionalized carbon nanotubes, ACS Nano **15**, 923 (2021).

[93] F. Wegner, Inverse participation ratio in 2 + e dimensions, Z. Phys. B **36**, 209 (1980).

[94] N. C. Murphy, R. Wortis, and W. A. Atkinson, Generalized inverse participation ratio as a possible measure of localization for interacting systems, Phys. Rev. B **83**, 184206 (2011).

[95] D. Hu and P. Huo, *Ab initio* molecular cavity quantum electrodynamics simulations using machine learning models, J. Chem. Theor. Comput. **19**, 2353 (2023).

[96] D. T. Colbert and W. H. Miller, A novel discrete variable representation for quantum mechanical reactive scattering via the *s*-matrix Kohn method, J. Chem. Phys. **96**, 1982 (1992).

[97] P. J. Reynolds, R. N. Barnett, B. L. Hammond, and W. A. Lester, Molecular physics and chemistry applications of quantum Monte Carlo, J. Stat. Phys. **43**, 1017 (1986).

[98] A. H. Kulahlioglu and A. Dreuw, The multistate quantum Monte Carlo algebraic diagrammatic construction method, J. Phys. Chem. A **127**, 2161 (2023).

[99] C. J. Umrigar, J. Toulouse, C. Filippi, S. Sorella, and R. G. Hennig, Alleviation of the fermion-sign problem by optimization of many-body wave functions, Phys. Rev. Lett. **98**, 110201 (2007).

[100] J. Kim, A. D. Baczewski, T. D. Beaudet, A. Benali, M. C. Bennett, M. A. Berrill, N. S. Blunt, E. J. L. Borda, M. Casula, D. M. Ceperley, S. Chiesa, B. K. Clark, R. C. Clay, K. T. Delaney, M. Dewing, K. P. Esler, H. Hao, O. Heinonen, P. R. C. Kent, J. T. Krogel *et al.*, QMCPACK: an open source *ab initio* quantum Monte Carlo package for the electronic structure of atoms, molecules and solids, J. Phys.: Condens. Matter **30**, 195901 (2018).